



# Fabrication of Fe-doped ZnO/nanocellulose nanocomposite as an efficient photocatalyst for degradation of methylene blue under visible light

Mohammad Saeed Vasheghani Farahani · Maryam Nikzad ·  
Mohsen Ghorbani

Received: 6 November 2021 / Accepted: 26 June 2022 / Published online: 6 July 2022  
© The Author(s), under exclusive licence to Springer Nature B.V. 2022

**Abstract** In this work, a photocatalytic nanocomposite, Fe-doped ZnO/nanocellulose, was synthesized using an in-situ method and examined for methylene blue (MB) degradation. For this purpose, pure ZnO (PZ) was synthesized by the chemical precipitation method and then subjected to Fe<sup>3+</sup> doping with different concentrations of Fe<sup>3+</sup> (1, 3, and 5 mol%). The PZ and Fe-doped ZnO (FZ) samples were characterized using several standard analyses. UV–Vis DRS analysis was also used to investigate the effect of Fe<sup>3+</sup> doping on the bandgap of PZ. The doping of Fe<sup>3+</sup> enhanced the photocatalytic activity of ZnO under visible light. The degradation efficiency of FZ samples (> 50%) was enhanced compared to the pristine ZnO (36.91%) during the same period. The catalyst with the highest degradation efficiency (94.21%) was then conjugated with broom corn stalk-derived

nanocellulose (NC) at varying NC/Zn<sup>2+</sup> molar ratios (0.1, 0.2, 0.3, and 0.4) and characterized by various analyses. The NC enhanced the hydroxyl group at the surface of the nanocomposite, consequently improved the photocatalytic performance of the synthesized samples. The ability of the optimized photocatalyst for MB degradation was assessed. The effect of operating parameters such as pH, catalyst dosage, and initial MB concentration was investigated and degradation efficiency of 98.84% was achieved at the optimum condition. Besides, photocatalyst regeneration study indicated the great photocatalytic performance of this nanocomposite with no loss in its degradation efficiency. The facile synthesis and fast degradation rate of this nanocomposite make it a promising candidate for real-world wastewater treatment.

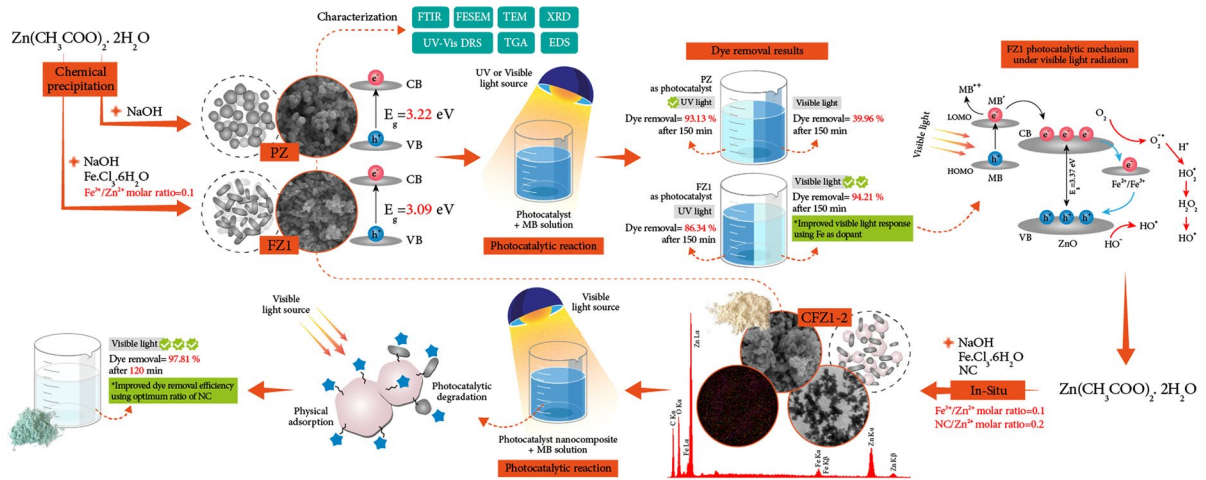
---

**Supplementary Information** The online version contains supplementary material available at <https://doi.org/10.1007/s10570-022-04735-y>.

---

M. S. Vasheghani Farahani · M. Nikzad (✉) ·  
M. Ghorbani  
Faculty of Chemical Engineering, Babol Noshirvani  
University of Technology, Babol, Iran  
e-mail: m.nikzad@nit.ac.ir

## Graphical abstract



**Keywords** Nanocellulose · Broom corn stalk · Photocatalytic degradation · Methylene blue · Fe-doped ZnO

## Introduction

Over the past few decades, the discharge of industrial effluents into water bodies has raised environmental concerns (Nagaraju et al. 2020). Dyes are one of the most prominent pollutants that display an increasing ecological threat. Different industries such as textile, leather tanning, plastics, cosmetics, and paint production are among the largest producers of colored effluents and create severe environmental pollution problems (Rajendran et al. 2020; Sirajudheen et al. 2020). Dyes are non-biodegradable compounds that reduce the aquatic plants' photosynthetic activity by preventing the penetration of light into the water and also contaminate the food chain because of their toxicity (Elfeky et al. 2020). Therefore, to keep the environment safe, it is necessary to remove dyes from contaminated effluents before being discharged to water resources.

Several conventional approaches consisting of flocculation-coagulation (Wang et al. 2020), membrane separation (Yang et al. 2020), adsorption (Saxena et al. 2020), biological treatment (Masoudnia et al. 2020), and ozonation (Muniyasamy et al. 2020) have been used to remove dyes from aqueous solutions and industrial wastewaters. However, these methods need additional treatment to avoid secondary

pollution (Emadian et al. 2020). Recently, advanced oxidation processes (AOPs) have been widely used for wastewater treatment (Abebe et al. 2020; Wang et al. 2019; Qi et al. 2017). Among AOPs, heterogeneous photocatalysis as an effective process has received great attention, thanks to its high efficiency, low cost, simple design, mild reaction condition, and environmental-friendliness (Chand et al. 2020; Flores et al. 2020). Semiconductor metal oxides such as ZnO,  $TiO_2$ ,  $Fe_3O_4$ , CuO,  $SnO_2$ , and  $Bi_2O_3$  have been employed as photocatalyst in the wastewater treatment (Namini et al. 2021; Chand et al. 2020; Qi et al. 2020, 2017; Evdokimova et al. 2020; Ciciliati et al. 2015). Among them, ZnO has been extensively used in different applications because of its high catalytic activity, low cost, tunable morphology and non-toxicity (Kim and Yong 2021; Wahid et al. 2019). It has a wide bandgap of  $\sim 3.3$  eV and a high exciton binding energy of 60 meV at room temperature with noble photochemical, optoelectronic, and piezoelectric properties (Ba-Abbad et al. 2013). However, ZnO suffers from some drawbacks such as the massive charge carrier recombination, large bandgap, high surface energy, photoinduced corrosion-dissolution at an extreme value of pH and poor visible light harvesting which limit the overall photocatalytic efficiency (Türkyılmaz et al. 2017). Due to the large bandgap energy, ZnO can be only activated under UV light irradiation, which constitutes approximately 5% of solar radiation (Yu and Yu 2008). To this end, many efforts have been dedicated to develop visible

light active ZnO photocatalyst (Saffari et al. 2020; Sharma et al. 2020; Abdel-Wahab et al. 2016). Several strategies, such as tailoring the intrinsic defects, doping with transition metals and anionic non-metals, surface modification with organic compounds, noble metal deposition, hetero structuring with other semiconductors and modification with carbon nanostructures, have been successfully used to improve the photoactivity and stability of ZnO (Kumar and Rao 2015). Doping of ZnO with transition metals has been reported as an effective approach to improve ZnO photocatalytic properties under visible light (Qi et al. 2020; Shahbazkhany et al. 2020; Türkyılmaz et al. 2017). Fe-doped ZnO exhibited better photocatalytic activity than pure ZnO under visible light in many studies (Kouhail et al. 2022; Isai and Shrivastava 2019; Ciciliati et al. 2015). This metal is one of the most common elements. Fe ion could act as a shallow electron trap in the lattice of photocatalyst that reduces the electron–hole recombination rate and enhances photocatalytic activity (Lavand and Malghe 2018). Hence, Fe was selected as the doping ion in this research.

Despite being an excellent photocatalyst due to their large surface area and high surface energy, ZnO nanoparticles (NPs) tend to aggregate, resulting in reduction of their light absorption which largely limits their photocatalytic activity (Jiang et al. 2020). These nanoparticles are prone to elution in a flowing system. There are also difficulties in separating and recovering the spent catalyst and post-treatment of the effluent stream. These limitations can be overcome by immobilizing the Fe-doped ZnO nanoparticles onto a suitable substrate. To overcome this challenge, nanocomposites consisting of ZnO incorporated into natural polymers, such as cellulose (Abdalkarim et al. 2018), lignin (Zhang et al. 2020), chitosan (Kamal et al. 2015), and their derivatives (Jiang et al. 2020; Lizundia et al. 2018) have been developed. Cellulose is the most abundant, sustainable and renewable biopolymer that has been extensively employed in the synthesis of polymer nanocomposites (Ganguly and Lim 2020). It has attracted increasing attention, especially at nanoscale. Nanocellulose (NC), a promising natural material isolated from lignocellulosic materials, has excellent unique surface chemistry, physical properties, non-toxicity, biodegradability, and biocompatibility (Jiang et al. 2020). High

concentration of hydroxyl groups on NC surface which can complex well with metal cations results in the homogenous dispersion of metal nanoparticles onto the NC matrix (Nang An et al. 2020). Besides, surface modification of NC using sulfuric acid creates sulfate ester groups which replace hydroxyl groups and provide a highly charged surface that can act as an excellent template for the dispersion of  $Zn^{2+}$  to prevent its aggregation (Ghasemlou et al. 2021; Moon et al. 2011). In addition, using NC as a substrate to support metal nanoparticles is beneficial for the recovery of catalyst, which can increase the adsorption properties and accelerate the catalytic degradation of pollutants (Li et al. 2020). Recently, several studies reported the application of cellulose as a matrix for the fabrication of ZnO/cellulose composites (Elfeky et al. 2020; Fu et al. 2017; Lefatshe et al. 2017). The addition of metal oxide nanoparticles onto the nanocellulose structure is extremely interesting as it may not only prevent the aggregation of the ZnO nanoparticles, but may also lead to the manufacture of a new class of cellulose based multifunctional hybrid materials (Ghasemlou et al. 2021). It has been shown that the hybridization of ZnO with NC improved its photocatalytic performance. Lefatshe et al. synthesized NC from oil palm empty fruit and used it as a host polymer for the fabrication of ZnO/cellulose nanocomposite. Results indicated that this nanocomposite exhibited a higher photocatalytic activity than pure ZnO nanostructure for the degradation of methylene blue (MB) (Lefatshe et al. 2017). Li et al. prepared ZnO/cellulose nanocomposites with adjustable photocatalytic properties. They used cellulose fibers with different aspect ratios and sizes for controlling the morphology of ZnO. They obtained ZnO with sheet, sphere, and flower-like morphologies via *in-situ* synthesis of cellulose fibers by a chemical deposition method. They found the flower-like ZnO supported on cellulose fiber displayed the best photocatalytic activity (Li et al. 2021a, b). Guan et al. used bamboo crystalline nanocellulose (CNC) as a template for the fabrication of ZnO/CNC hybrid nanocomposite with modulated morphologies. They prepared this nanohybrid photocatalyst by a green one-step synthesis approach and investigated the effect of pH values on the morphology, thermal stability, antibacterial efficiency and dye removal efficiency of the photocatalyst. Their

results showed that the fabricated nanocomposite displayed higher thermal stability and removal efficiency than pure CNC (Guan et al. 2019). Although reports on the development of ZnO/nanocellulose composites as photocatalysts are numerous, additional doping of this nanocomposite to further improve its photocatalytic activity has been rarely reported. Li et al. prepared porous Al-doped ZnO-cellulose composite. They investigated the effect of cellulose fiber size on the composite structure and showed its important role in the photocatalytic properties of fabricated composite (Li et al. 2020). Xiao et al. prepared Fe/ZnO composite nanosheets by hydrothermal technique using nanofibrillated cellulose (NFC) as a template and then employed it for photocatalytic degradation of tetracycline in aqueous solution. Their results showed that the synthesized nanocomposites displayed superior physical adsorption and photodegradation efficiency than ZnO/NFC under UV light irradiation (Xiao et al. 2017). Nasiri et al. incorporated Au/ZnO nanoparticles into cellulose acetate (CA) matrix using phase inversion process. They studied the effect of Au/ZnO nanoparticles on the morphology of cellulose-based nanocomposite. They reported that the porosity of CA/Au/ZnO nanocomposite was higher than the pure CA and the synthesized CA/Au/ZnO nanocomposite degraded Eosin Y, while no photocatalytic activity was obtained for the pure CA (Abad et al. 2020). The synthesis of new supporting materials with diverse physiochemical characteristics got immense interest in the scientific fields. As mentioned above, several researches reported the cellulose and cellulose derivatives as matrix for pure and metal-doped ZnO in the preparation of multifunctional nanocomposites. Although research on cellulose nanocomposites is exponentially growing, there are few published studies on the synthesis of pure and metal-doped ZnO NPs on nanocellulose matrix. Despite the elucidated role of Fe doping on ZnO and incorporation into the nanocellulose as host matrix on photocatalytic performance of ZnO, only one study (Xiao et al. 2017) has been undertaken to fabricate Fe-doped ZnO/nanocellulose to the best of our knowledge.

In this study, we aimed to investigate the photocatalytic activity of metal-biopolymer nanocomposite materials and designed a high-efficiency Fe-doped ZnO/nanocellulose (CFZ) composite as

a new nanocomposite for MB degradation under visible light. To the best of authors' knowledge, there is no report on the fabrication of CFZ nanocomposite through in-situ precipitation technique and the influence of NC concentration on the photocatalytic performance of the nanocomposite. The use of bottom-up in situ synthesis for the fabrication of the nanocomposite is advantageous compared to the top-down ex situ mixing method, as it offers increased control over the structure and properties of the material by incorporating particle generation, surface modification, and integration into the polymer matrix in one process. The simultaneous presence of NC as a matrix and carrier for stabilization of metal ions through electrostatic interaction and occurrence of Fe-doped ZnO precipitation can produce CFZs with good structural properties. In this work, broom corn stalk was used as feedstock for NC isolation. The NC and Fe-doped ZnO (FZ) were synthesized by acid hydrolysis and precipitation methods, respectively. The structural and morphological characteristics of the isolated NC, FZ and CFZ nanocomposite were determined by FTIR, FESEM, XRD, TEM, UV-Vis DRS, and TG analyses. The photocatalytic activity of these materials for the degradation of MB, as the target pollutant, in the aqueous solution was examined. Moreover, the influence of different parameters such as pH, photocatalyst dosage, and initial dye concentration on the degradation of MB by CFZ composite was investigated. In addition, the regeneration study was conducted to confirm the excellent performance of the fabricated nanocomposite.

## Materials and methods

### Materials

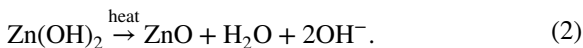
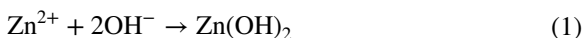
The lignocellulosic feedstock used for NC isolation and its composition is described in the Supporting Information, Section S1.1. Zinc acetate dihydrate ( $\text{Zn}(\text{CH}_3\text{CO}_2)_2 \cdot 2\text{H}_2\text{O}$ ), iron trichloride hexahydrate ( $\text{FeCl}_3 \cdot 6\text{H}_2\text{O}$ ), sulfuric acid ( $\text{H}_2\text{SO}_4$ ), sodium hydroxide ( $\text{NaOH}$ ), sodium chlorite ( $\text{NaClO}_2$ ), sodium carbonate ( $\text{Na}_2\text{CO}_3$ ), ethanol ( $\text{C}_2\text{H}_5\text{OH}$ ), methylene blue (MB), and other chemicals were purchased from Merck (Darmstadt, Germany). All the required chemicals were analytical grade and used as received without further purification.

### Isolation of nanocellulose from BS

Details of the nanocellulose isolation are described in the Supporting Information, Section S1.2. In addition, the schematic presentation of the NC isolation from broomcorn stalk (BS) by acid hydrolysis process is depicted in Fig. S1.

### Preparation of ZnO and Fe/ZnO NPs

Pure ZnO and Fe/ZnO nanoparticles were prepared by the chemical precipitation method. Initially, the required stoichiometric amounts of  $\text{Zn}(\text{CH}_3\text{CO}_2)_2 \cdot 2\text{H}_2\text{O}$  and  $\text{FeCl}_3 \cdot 6\text{H}_2\text{O}$  were dissolved in 50 ml of deionized water depending on the percentage of Fe doping. The mixture was heated at 65 °C under constant magnetic stirring to obtain a homogeneous solution. Thereafter, about 50 ml of 1 M NaOH solution was added dropwise to the solution to attain pH 10, under continual stirring at 65 °C for 1 h. Meanwhile, the color of the solution changed from white or brown (depending on the iron content) to milky white, which indicates the conversion of  $\text{Zn}^{2+}$  to  $\text{Zn}(\text{OH})_2$  according to Eq. (1) (Türkyılmaz et al. 2017; Akir et al. 2016). The resulting samples were centrifuged at 6500 rpm for 15 min and subsequently washed several times with deionized water to remove residual and unwanted impurities. Eventually, to convert the  $\text{Zn}(\text{OH})_2$  to ZnO (Eq. (2)), the precipitates were oven-dried at 100 °C for 12 h. In this way, Fe-doped ZnO nanoparticles with different concentrations of  $\text{Fe}^{3+}$  (0, 1, 3, and 5 mol%) were prepared and denoted as PZ, FZ1, FZ3, and FZ5, respectively.



### Fabrication of Fe-doped ZnO/nanocellulose nanocomposite

An in situ technique was used for the fabrication of the Fe-doped ZnO/nanocellulose nanocomposite. For this purpose, 2.2 g of  $\text{Zn}(\text{CH}_3\text{CO}_2)_2 \cdot 2\text{H}_2\text{O}$  and 0.027 g of  $\text{FeCl}_3 \cdot 6\text{H}_2\text{O}$  (mole ratio 1:0.01) were dissolved in 50 ml of deionized water and then heated to 65 °C under constant stirring. Afterwards, a specific amount of NC was added to the previous solution to

obtain different NC/ $\text{Zn}^{2+}$  molar ratios (0.1, 0.2, 0.3, and 0.4) under constant stirring of 500 rpm for 1 h. Subsequently, the mixture was sonicated, using an ultrasonic water bath (Easy 30 H, Elma, Germany) for 1 h to achieve a homogenous blend. Then, about 50 ml of 1 M NaOH solution was added dropwise under constant stirring to attain pH 10. The samples were centrifuged and rinsed several times with distilled water to remove impurities. Finally, the product was oven-dried at 100 °C for 12 h. The fabricated nanocomposites were labelled as CFZ1-1, CFZ1-2, CFZ1-3, and CFZ1-4 which represent different NC/ $\text{Zn}^{2+}$  molar ratios of 0.1, 0.2, 0.3, and 0.4, respectively.

### Sample characterization

The functional groups of the developed samples were characterized using an FTIR spectrometer (WQF-520, China). The crystalline phase and crystallite size of samples were determined by XRD spectroscopy using a Philips PW 1730 X-ray diffractometer with Cu radiation source ( $\lambda = 1.5406 \text{ \AA}$ ). The used accelerating voltage and tube current were 40 kV and 30 mA, respectively. The scanning of samples was recorded in the diffraction angle ( $2\theta$ ) range of 5°–80°. The surface and structural morphology of the synthesized samples were analyzed by TEM (Philips CM120, Germany) and FESEM (TESCAN MIRA, Czech) equipped with energy dispersive spectroscopy (EDS) for elemental composition analysis. The optical transmittance of PZ, FZs and CFZs was measured using UV–Vis DRS (Shimadzu UV-160 A, China) in the range of 190–1100 nm. The thermal decomposition behavior of the samples was monitored by TGA and DTG analyses using a Mettler Toledo apparatus. The heating was carried out under  $\text{N}_2$  atmosphere at a flow rate of 200 mL/min and a heating rate of 10 °C/min in the range of 25–600 °C. The photocatalytic degradation of MB was determined by absorbance measurement using a UV–visible spectrophotometer (Unico 2800, USA) at 664 nm.

### Photocatalytic study

The photocatalytic performance of the samples was analyzed by investigating the degradation of MB as

a model pollutant. A 6 W UV-C lamp (254 nm) and a 250 W high-pressure mercury lamp equipped with a UV-cut filter (<400 nm) were used as UV and visible irradiation sources, respectively. In a typical photocatalytic experiment, 0.1 g of the sample (PZ, FZs, or CFZs) was added to 100 ml of 5 ppm MB solution. Then, the mixture was stirred and kept in the dark place prior to the photocatalytic reaction for 30 min to ensure the establishment of an adsorption and desorption equilibrium (Ali et al. 2021). Subsequently, the mixture was irradiated under UV or visible light for photodegradation of MB. During the reaction, aliquots were taken from the solution at regular intervals. To separate the catalyst from the solution, the samples were centrifuged at 6500 rpm for 30 min and the dye concentration was analyzed. The photocatalytic degradation efficiency of MB was calculated using Eq. (3).

$$\text{Degradation \%} = \frac{(C_0 - C_t)}{C_0} \times 100 \quad (3)$$

where  $C_0$  is the initial dye concentration in the solution and  $C_t$  is the concentration of dye at any time. The influence of experimental parameters such as solution pH (3, 5, 7, 9, and 11), catalyst dosage (0.5, 1.0, 1.5, and 2.0 g/L), and initial MB concentration (5, 10, 15, 20, and 25 ppm) on its degradation by the best-performing catalyst was investigated. After photocatalytic reaction under the optimum condition, the CFZ1-2 and FZ1 were separated and washed with

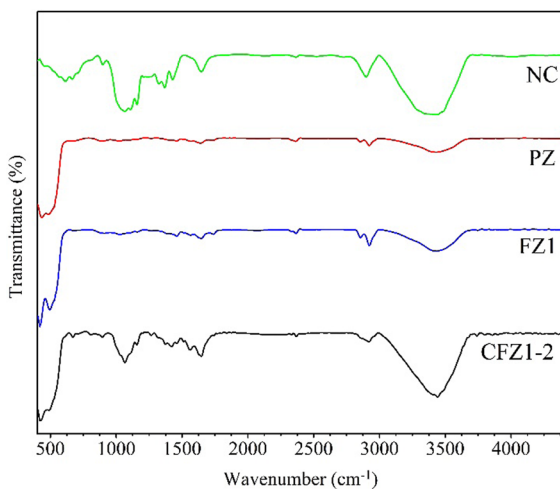


**Fig. 1** FTIR spectra of NC, PZ, FZ1, and CFZ1-2

distilled water for reuse in the next run of MB photodegradation under the same condition. The regeneration tests of these samples were done 4 times.

## Results and discussion

### FTIR analysis

The FTIR spectra of BS and bleached BS (BBS) are exhibited in Fig. 2S, and the corresponding discussion is presented in the Supporting Information, Section S2.1. The FTIR spectra of NC, PZ, FZ1, and CFZ1-2 were scanned in the range of 4000–400  $\text{cm}^{-1}$  and the recorded spectra are illustrated in Fig. 1. The broadbands observed at 3408  $\text{cm}^{-1}$  in all samples belong to the stretching vibration of O–H and the peak at 1646  $\text{cm}^{-1}$  is attributed to the absorbed water molecules by the samples (Langari et al. 2019). These peaks show the hydrophilic tendency of all samples. The FTIR spectra of NC, PZ, FZ1, and CFZ1-2 are presented in Fig. 3b. The characteristic peaks around 430–500  $\text{cm}^{-1}$  correspond to metal–oxygen vibration, which are observed in the spectra of PZ, FZ1 and CFZ1-2. It is worth noting that the characteristic peaks of FZ1 are similar to those of PZ, indicating that the doped Fe into ZnO existed in the form of elements. Similar characteristic peaks of NC were observed in the spectrum of CFZ1-2 composite. Moreover, compared with NC, a new absorption peak at 400–500  $\text{cm}^{-1}$  assigned to Zn–O or Fe–O stretching vibration was found in the CFZ1-2 composite (Guan et al. 2019). Furthermore, it could be seen that the intensity of these characteristic peaks decreased in the spectrum of CFZ1-2. This reduction confirms the strong interaction between FZ particles and NC chains.

### Morphology and dimensions

The FESEM and TEM images of native BS, BBS, and isolated NC are shown in Fig. 3S, and the corresponding discussion is presented in the Supporting Information, Section S2.2. Figure 2 displays the FESEM, TEM, and statistical graph of particle size distribution  $n$  of as-prepared samples. Figure 2a<sub>1</sub>–a<sub>4</sub> show the surface morphologies of the pristine and Fe-doped ZnO. As shown in the FESEM images, the average size of the particles was in the nanometer

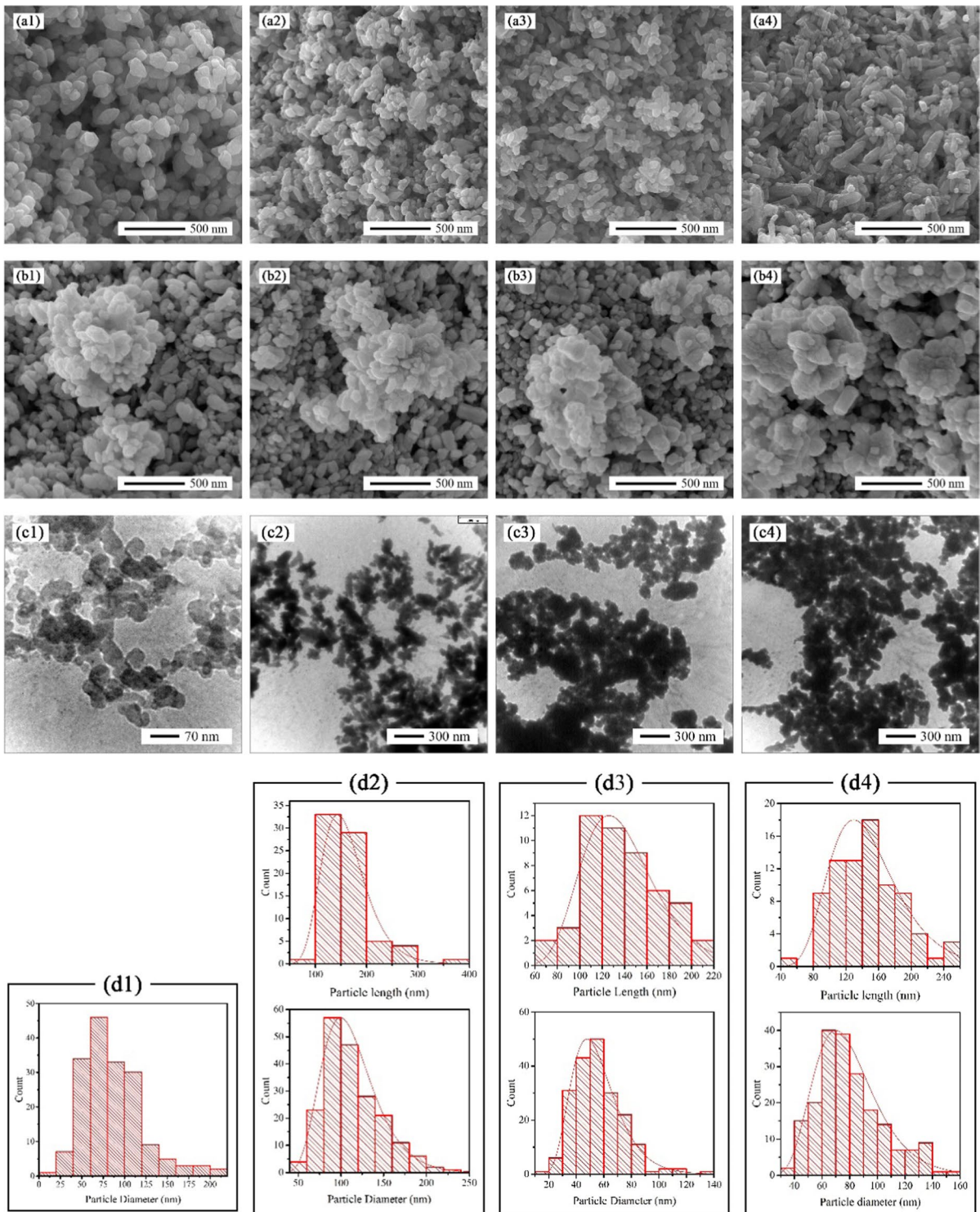


**Fig. 2** **a**<sub>1</sub>–**a**<sub>4</sub> FE-SEM images of PZ, FZ1, FZ3, and FZ5, respectively. **b**<sub>1</sub>–**b**<sub>4</sub> FE-SEM images of CFZ1-1, CFZ1-2, CFZ1-3, and CFZ1-4, respectively, **c**<sub>1</sub>–**c**<sub>4</sub> TEM images of NC,

PZ, FZ1, and CFZ1-2, respectively, and **d**<sub>1</sub>–**d**<sub>3</sub> the histogram of particle length and diameter distribution of PZ, FZ1, and CFZ1-2, respectively

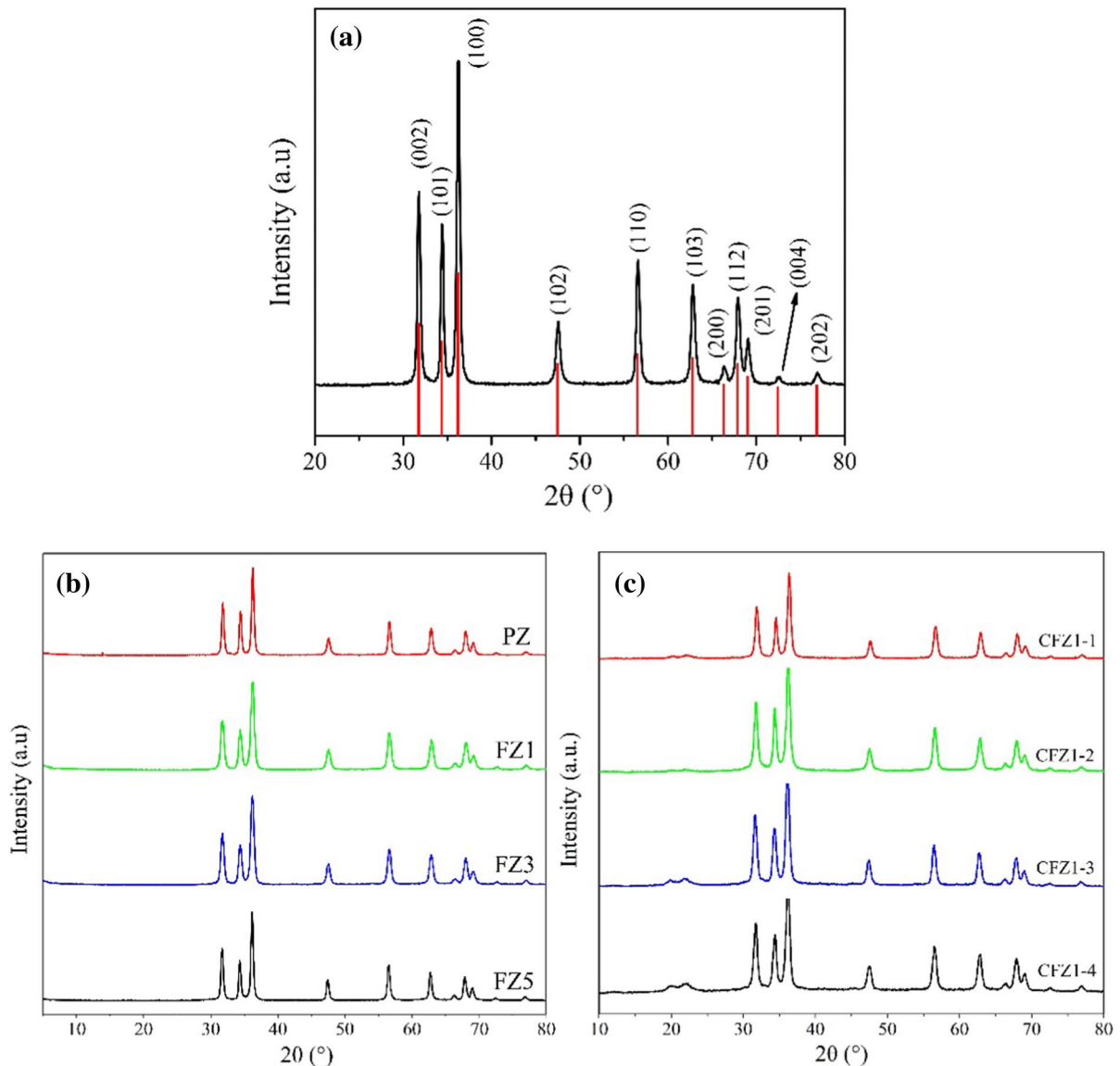


**Fig. 3** XRD patterns of **a** PZ, **b** FZs, and **c** CFZs

range. It is evident from Fig. 2a<sub>1</sub> that PZ sample presented a nearly zero-dimensional (0D) growth with the diameter of 100 nm and Fe<sup>3+</sup> doping affected the growth direction and the shape of the synthesized nanoparticles. In the FZ1, FZ3, and FZ5 samples, the 0D growth of PZ gradually turned into 1D growth and the particle length increased to 130 ± 10, 140 ± 10, and 150 ± 10 nm, respectively. The particle diameter was slightly influenced by the dopant concentration. As the dopant concentration increased from 1 to 5%, the diameter decreased from 50 ± 10 to 30 ± 10 nm.

The surface morphology of CFZ hybrid nanocomposites is shown in Fig. 2b<sub>1</sub>–b<sub>4</sub>. As can be seen, by the addition of NC during the synthesis of FZ1, the average diameter of nanocomposite increased to 70 ± 10, 75 ± 10, 85 ± 10, and 100 ± 10 nm for CFZ1-1, CFZ1-2, CFZ1-3, and CFZ1-4 samples, respectively. Besides, due to the greater tendency of NC to form a precipitate, with increasing its content in the nanocomposite, larger sediments were observed in the nanocomposites.



Figure 2c<sub>1</sub>–c<sub>4</sub> display the TEM images of NC, PZ, FZ1, and CFZ1-2, respectively. The image of the NC sample clearly revealed that the particle size distribution of NC was in the range of 20 to 150 nm, which were scattered next to each other (Fig. 2c<sub>1</sub>). The TEM image of PZ sample evidently exhibited the nearly spherical morphology of the nanoparticles (Fig. 2c<sub>2</sub>). It is clear that Fe<sup>3+</sup> doping changed the morphology of the PZ particles (Fig. 2c<sub>3</sub>). Further, the TEM image of CFZ1-2 composite illustrated in Fig. 3d4 identifies that the particles were fabricated with successful integration between Fe–ZnO and NC. Figure 2d<sub>1</sub>–d<sub>4</sub> indicate the histogram of particle length and diameter distribution of PZ, FZ1, and CFZ1-2, respectively.

### XRD analysis

The XRD analysis was carried out to identify the crystalline structure of the samples. The diffraction patterns of the BS and NC samples are shown in Fig. 4S, and corresponding results are discussed in the Supporting Information, Section S2.3. The XRD patterns of PZ and FZs are shown in Fig. 3a–c. As shown in the XRD patterns, PZ and FZs samples displayed many intense peaks at  $2\theta = 31.78^\circ$ ,  $34.41^\circ$ ,  $36.25^\circ$ ,  $47.53^\circ$ ,  $56.59^\circ$ ,  $62.83^\circ$ ,  $66.39^\circ$ ,  $67.64^\circ$ ,  $69.05^\circ$ ,  $72.53^\circ$ , and  $76.92^\circ$  which assigned to the (100), (002), (101), (102), (110), (103), (200), (112), (201), (004), and (202) planes of the hexagonal wurtzite structure, respectively, and resemble those

previously reported (Isai and Shrivastava 2019). On the basis of wurtzite structure, the PZ and FZs samples correspond to the standard data (JCPDS No.01-080-0074). Meanwhile, no additional peaks were detected in FZs patterns, which indicated that iron was well doped into the crystal phase of PZ. The XRD diffractograms of CFZs nanocomposite are illustrated in Fig. 3c. The CFZs patterns exhibited two-phase structures corresponding to FZ and NC. It can be deduced that the presence of NC did not alter the crystal structure of FZ, and Fe-doped ZnO was crystallized well in the NC polymeric matrix, as no new peaks were detected.

The average crystallite size (*D*) of the PZ, FZs and CFZs was calculated using the Scherrer formula as:

$$D = \frac{0.89\lambda}{\beta \cos \theta} \quad (4)$$

where  $\lambda$  is the wavelength of the X-ray radiation (0.15406 nm),  $\beta$  is the full width at half maximum (FWHM) measured in radians, and  $\theta$  is the Bragg diffraction angle.

The (110) peak, the most intense peak for PZ, FZs, and CFZs samples, was used for the calculation of the crystallite sizes. The calculated crystallite size for PZ, FZs, and CFZs is summarized in Table 1. The average crystallite size of PZ was 17.8 nm. Results showed that the Fe-doped ZnO nanoparticles with higher content of Fe revealed smaller average crystallite sizes. Results showed that the substitution of Fe<sup>3+</sup> (0.64 Å) in place of Zn<sup>2+</sup> (0.74 Å) in zinc oxide lattice reduced the growth rate of zinc oxide crystallites as observed in other studies (Xiao et al. 2018; Ciciliati et al. 2015; Saleh et al. 2012). The average crystallite size of CFZ1-1, CFZ1-2, CFZ1-3, and CFZ1-4 was 12.7, 11.0, 9.1, and 8.2 nm, respectively. Compared to the crystallite size of FZ1, the crystallite size of CFZs reduced which is due to the inhibition of NC from the nucleation and growth of ZnO nanocrystals (Fabbiyola et al. 2016). Rich hydroxyl groups on the surface of the NC could generate strong electrostatic interaction with Zn ions, enabling the growth and dispersion of ZnO nanoparticles on NC. The NC as a matrix could disperse Fe-doped ZnO particles and further decrease the crystallite size of Fe-doped ZnO.

**Table 1** The calculated average crystallite size of PZ, FZs, and CFZs

Samples	Composition	Average crystallite size (nm)
PZ	Pure ZnO	17.8
FZ1	1% Fe doped ZnO	15.5
FZ3	3% Fe doped ZnO	14.4
FZ5	5% Fe doped ZnO	13.6
CFZ1-1	1% Fe doped + 0.1 NC blended ZnO	12.7
CFZ1-2	1% Fe doped + 0.2 NC blended ZnO	11.0
CFZ1-3	1% Fe doped + 0.3 NC blended ZnO	9.1
CFZ1-4	1% Fe doped + 0.4 NC blended ZnO	8.2

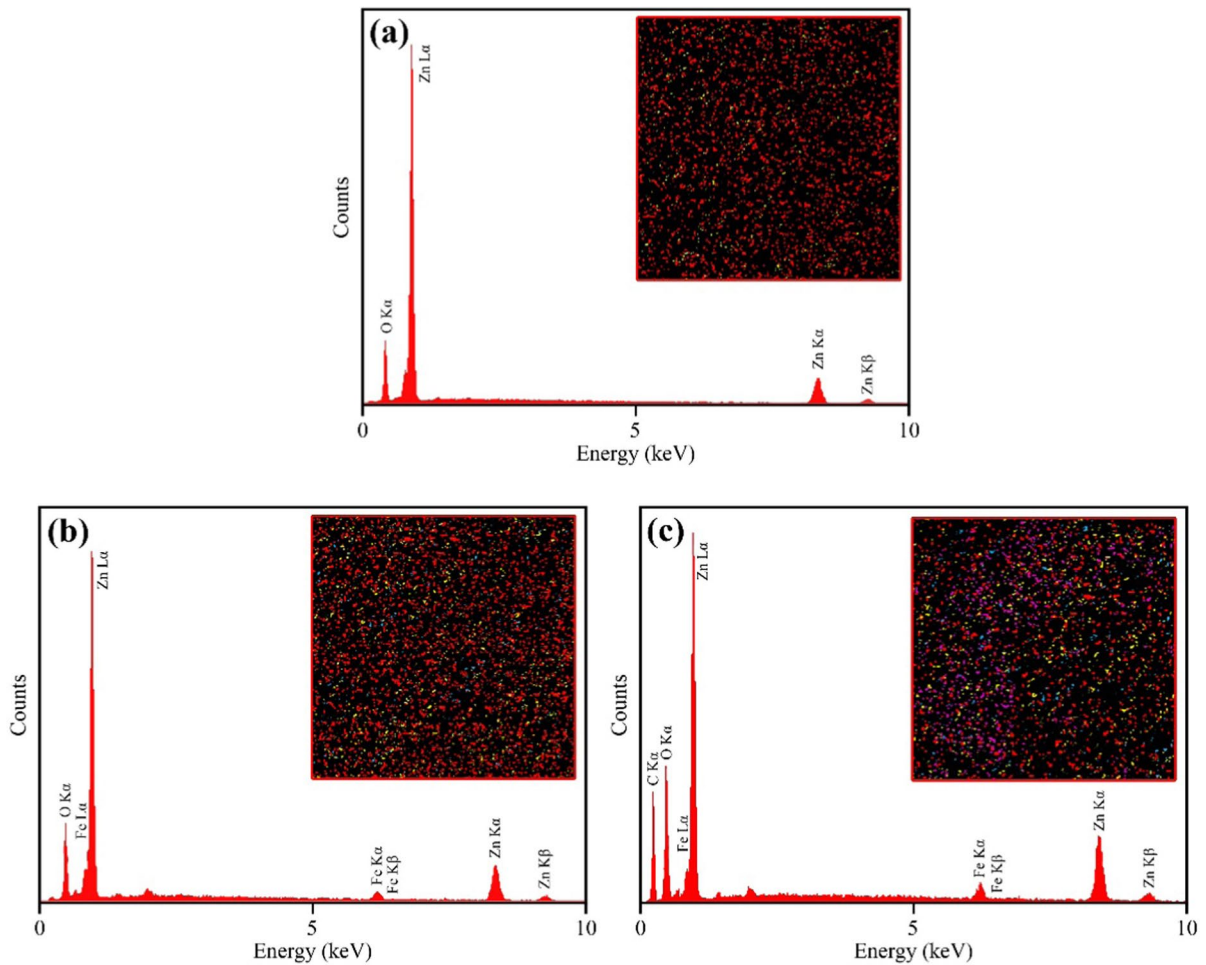


**Fig. 4** EDS spectra of **a** PZ, **b** FZ1, and **c** CFZ1-2. The insets show the elemental mapping: red (Zn), yellow (O), blue (Fe), magenta (C)

### EDS investigation

The EDS spectra of PZ, FZ1, and CFZ1-2 are shown in Fig. 4a–c. Table 2 presents the elemental composition of the prepared samples estimated by EDS.

**Table 2** Elemental composition obtained from EDS analysis of PZ, FZ1, and CFZ1-2

Samples	Elements			
	Zn (wt%)	O (wt%)	Fe (wt%)	C (wt%)
PZ	72.98	27.02	–	–
FZ1	69.95	29.40	0.65	–
CFZ1-2	49.87	32.12	0.69	17.32

The EDS spectrum of PZ shows peaks for zinc (Zn) and oxygen (O). The results reveal that the PZ sample consists of Zn and O with 72.98 and 27.02 wt%, respectively. Figure 4b displays peaks for Zn, O, and Fe with 69.95, 29.40, and 0.65 wt%, respectively. In addition, the distribution of Fe element in the FZ1 sample in Fig. 4b is very uniform, which indicates that the synthesis technique was reliable for the doping process. Figure 4c exhibits that the CFZ1-2 consists of Zn, O, Fe, and C with weight percentages of 49.87, 32.12, 0.69, and 17.32%, respectively. According to the mapping image (as depicted in the inset of Fig. 4c), Zn and Fe elements were uniformly distributed in CFZ1-2 nanocomposite. Therefore, nanocellulose was the desired substrate for dispersing

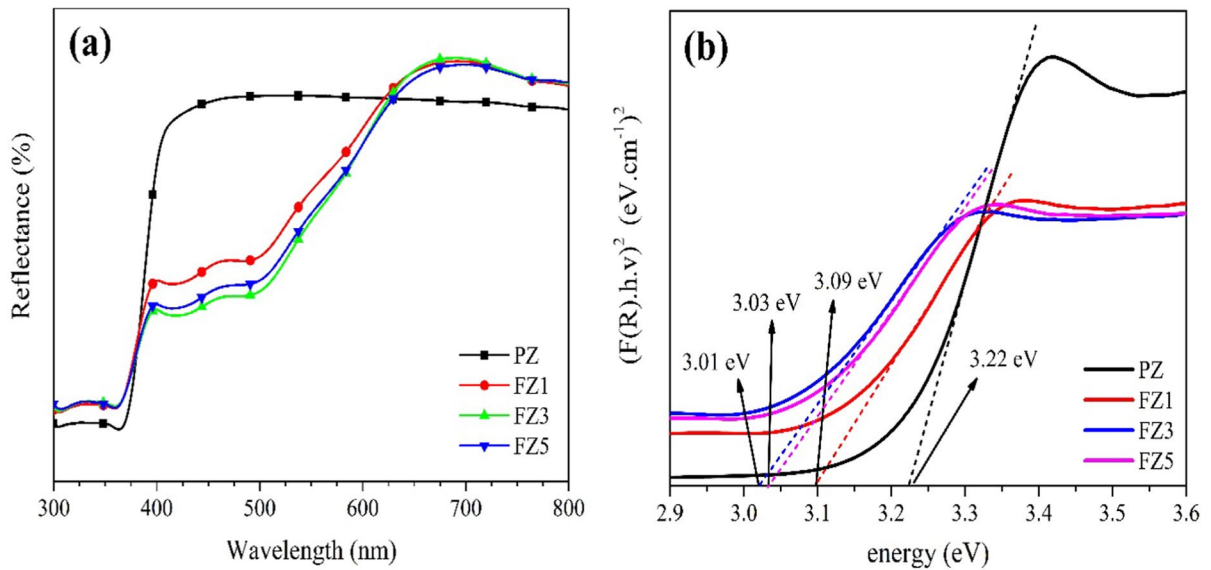


**Fig. 5** **a** Diffuse reflectance spectra and **b** Kubelka–Munk transformed reflectance spectra of PZ, FZ1, FZ3, and FZ5

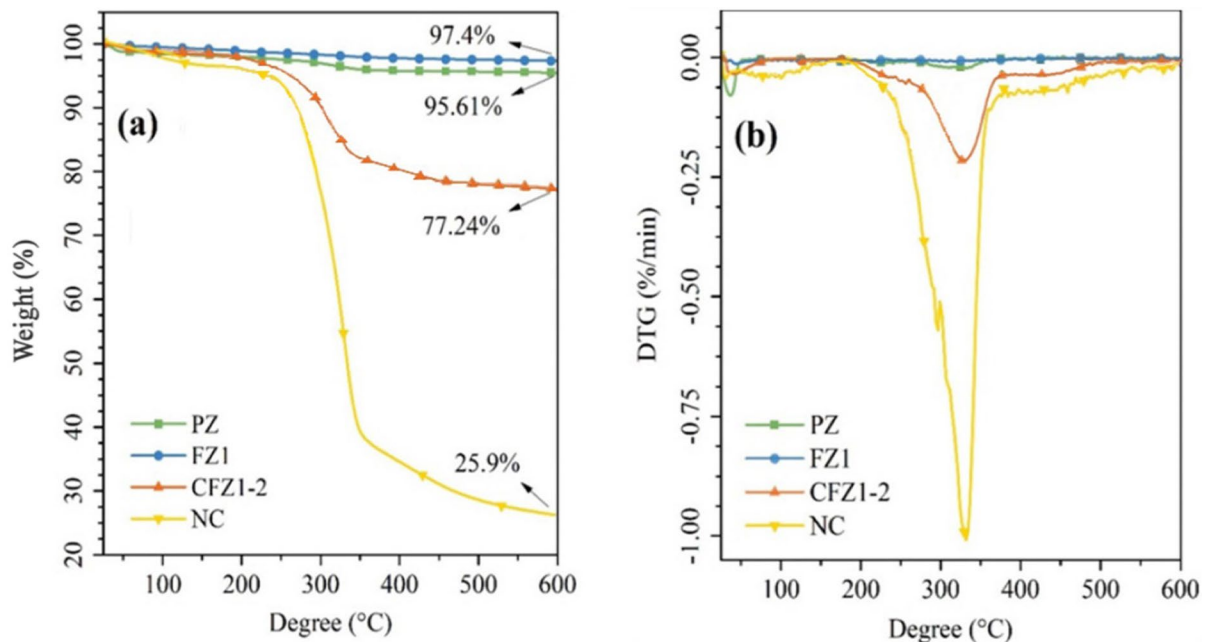


**Fig. 6** **a** TGA and **b** DTG profiles of NC, PZ, FZ1, and CFZ1-2

photocatalysts such Fe-doped ZnO. This result is consistent with previous studies (Shi et al. 2021).

#### UV–Vis DRS analysis and bandgap study

The influence of Fe<sup>3+</sup> doping on optical properties of ZnO was studied using UV–Vis DRS analysis. The diffuse reflectance spectra of the pure ZnO and

FZs are displayed in Fig. 5a. It was observed that the pristine ZnO nanoparticles exhibited a low diffuse reflectance at wavelengths less than 400 nm, which corresponds to an intense absorption peak between 200 to 400 nm. This result indicates that the PZ can efficiently absorb UV light. Compared to the pure ZnO, the FZs samples had lower diffuse reflectance in the visible region. On the other hand, Fe-doped samples were able to efficiently absorb visible light (solar light) for the photocatalytic process. Additionally, the bandgap energy of all samples was calculated from the well-known Kubelka–Munk (KM) equation and the plots are illustrated in Fig. 5b. The calculated bandgap energy of the FZ1, FZ3 and FZ5 samples are approximately 3.09, 3.03, and 3.01 eV, respectively, which is smaller than that of PZ (3.22 eV). This reduction could be attributed to the *s-d* and *p-d* exchange interactions between the band electrons and the d electrons of the Fe<sup>3+</sup> ions substituting Zn<sup>2+</sup> ions (Ciciliati et al. 2015).

#### Thermal stability

The TGA and DTG curves of NC, PZ, FZ1, and CFZ1-2 samples are depicted in Fig. 6. The PZ sample exhibited approximately 2.0% initial weight

loss below 100 °C, which corresponds to the evaporation of the adsorbed water on the surface of PZ nanoparticles. Then, subsequent weight loss of 4.3% occurred at 260–320 °C, which was attributed to the removal of organic components. The FZ1 sample displayed the highest thermal stability. A total weight loss of 2.6% was found for FZ1 sample. As observed, the thermal degradation of NC and CFZ1-2 samples took place in two stages. The first weight loss of 5% for NC sample occurred at about 250 °C; this was followed by a second weight loss of 60%, which happened at around 330 °C. The thermal weight loss of NC during this stage was mainly attributed to the depolymerization, dehydration, and decomposition of glycosyl units of NC sample. Compared with the NC sample, the thermal degradation peaks for CFZ1-2 were found at higher temperatures (290 and 350 °C). This was related to the stronger interactions between oxygen atoms of the NC and FZ1 nanoparticles that provide a thermal barrier for the NC skeleton. The TGA analysis showed a total weight loss of 22.76% for CFZ1-2. These results indicate that the thermal stability of CFZ1-2 was better than that of NC.

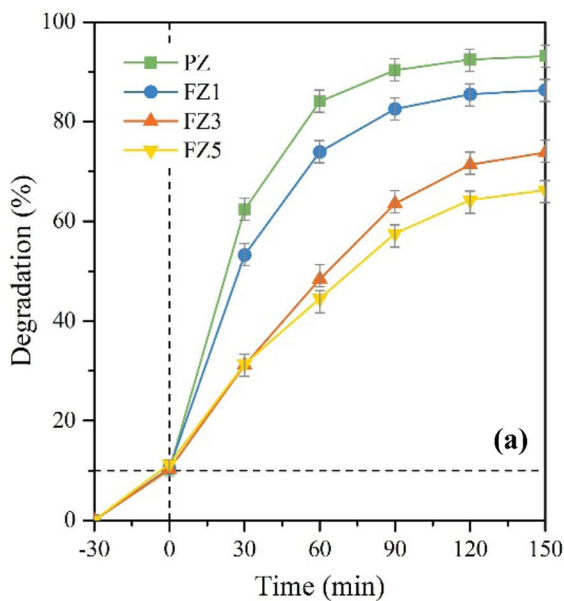
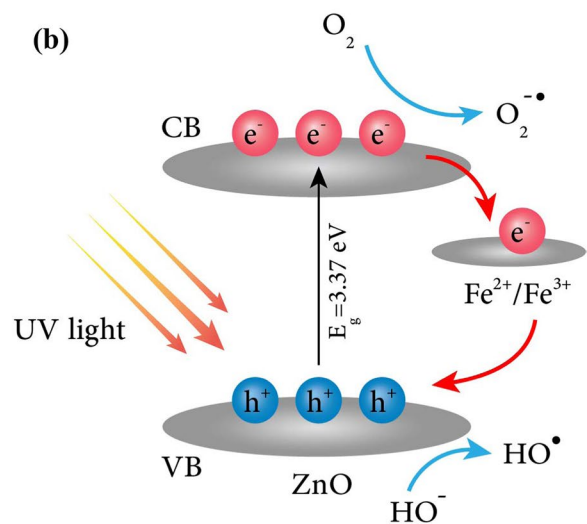
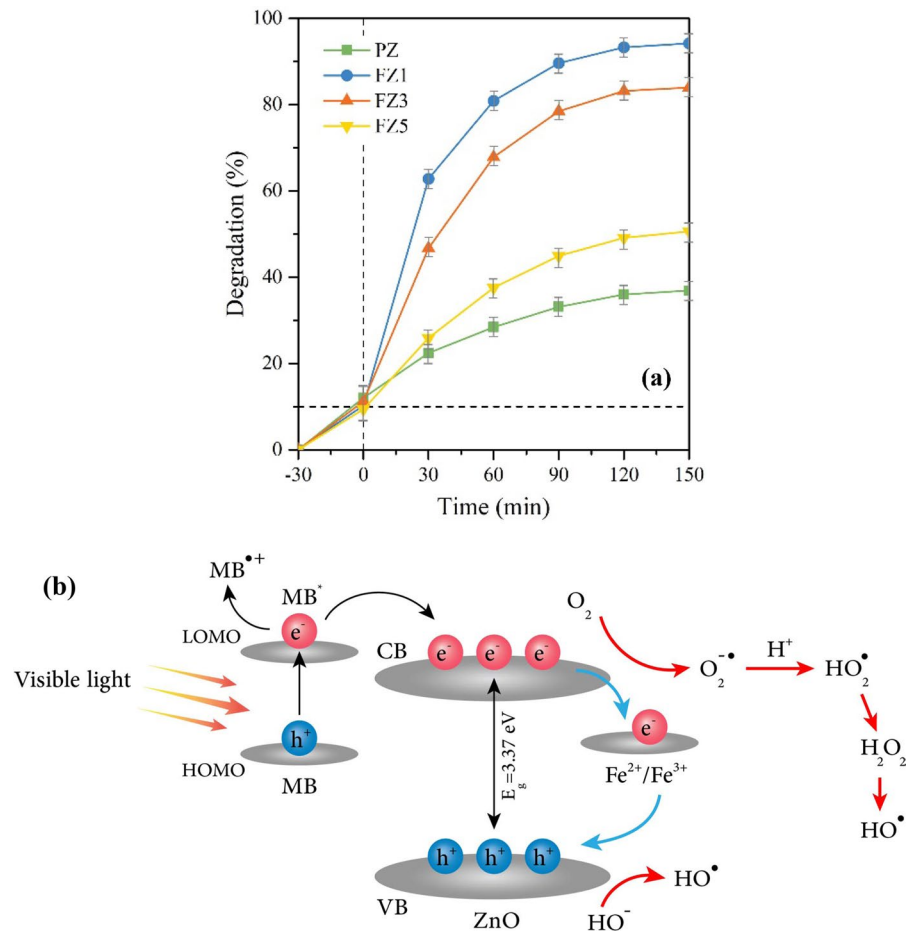


**Fig. 7 a** Photocatalytic degradation of MB in aqueous solution using the PZ and FZs under UV light radiation and **b** schematic representation of photocatalytic mechanism of Fe-doped



ZnO for MB degradation under UV light irradiation. Error bars indicate the standard deviation measured by three independent experiments

**Fig. 8 a** Photocatalytic degradation of MB in aqueous solution using the PZ and FZs nanoparticles under visible light radiation and **b** schematic representation of photodegradation mechanism of Fe-doped ZnO for MB under visible light irradiation. Error bars indicate the standard deviation measured by three independent experiments



### Photocatalytic degradation of MB

The photocatalytic activity of PZ and FZs was investigated in the MB degradation reaction, when exposed to both UV and visible light irradiations. In these experiments, the effect of iron ions in the photocatalysts on the degradation of MB was evaluated. In order to minimize the influence of adsorption of the synthesized catalyst, each experiment was performed in the dark condition for 30 min prior to the light irradiation. Figure 7a shows the photocatalytic degradation of MB in an aqueous solution with PZ and FZs nanoparticles under UV light radiation. It can be observed that the PZ sample degraded 93.13% of the MB dye in 150 min under UV light radiation, but the prepared Fe-doped samples exhibited lower photocatalytic activity. As the dopant molar ratio increased from 1 to 3 and 5%, the degradation of MB correspondingly decreased from 86.34 to 73.81

and 66.25%, respectively. The photocatalytic performance depends on different factors, such as the electron–hole recombination, average crystallite size, bandgap, and specific surface area (Roguai and Djelloul 2021a). According to the obtained results from XRD and UV–Vis analyses, the average crystallite size and bandgap of ZnO were influenced by Fe doping. It can be clearly seen that the enhancement of Fe dopant in ZnO nanoparticles decreased the average crystallite size and bandgap energy, which makes electron–hole recombination more easily. Thus, increasing the Fe dopant ratio reduces the photocatalyst activity under UV light irradiation by disrupting the redox process. This result is consistent with the previous studies (Roguai and Djelloul 2021b; Senthil Kumar and Arunagiri 2021; Yi et al. 2014). As shown in Fig. 7b, under UV light irradiation, the Fe ions in the ZnO crystal structure act as an electron–hole trap and promote the charge recombination.

Figure 8a illustrates the photocatalytic degradation of MB in an aqueous solution with PZ and FZs nanoparticles under visible light radiation. The degradation efficiency of MB over the PZ catalyst was 39.96% in 150 min of visible light irradiation. The pristine ZnO revealed poor photocatalytic performance under visible light irradiation compared to that under UV light irradiation. Similar results were reported by Yi et al. They observed pure ZnO showed strong photocatalytic properties while all Fe doped samples has lower performance under UV light irradiation. This could be attributed to the high band-gap of ZnO. As observed in Fig. 8a, the FZ1 catalyst exhibited the highest degradation efficiency of MB (94.21%), followed by FZ2 (83.97%) and FZ3 (50.62%). As expected, the increase of Fe<sup>3+</sup> doping ratio was very effective to enhance the performance of ZnO. A number of researches confirmed that the photocatalytic degradation efficiency of ZnO can be enhanced by doping with iron ions (Xiao et al. 2017; Yi et al. 2014). The difference in the transfer pathway of photogenerated electrons results in the different photocatalytic activity under the irradiation of UV and visible light because of the presence of Fe in the ZnO host. When the samples are irradiated by UV light, the Fe ions may act as traps for the photogenerated electrons and holes and promote the recombination; thus, the Fe/ZnO photocatalytic performance is reduced. Whereas, in the existence of visible light, the presence of Fe can facilitate separation and hinder recombination of photogenerated electron-hole pairs from excited MB. A scheme of plausible mechanism for the MB photocatalytic degradation over Fe-doped ZnO under visible light is displayed in Fig. 8b. The typical mechanism for the photodegradation of dyes was reported by Chiu et al. (2019). They introduced mechanism of direct photodegradation and sensitization-mediated degradation processes. In fact, based on dye molecule band positions, the generation of reactive species in semiconductor photocatalysts can directly degrade dye molecules. Alternatively, the self-photosensitization of dye may occur to improve the generation of reactive species when the CB photocatalysts are more negative than the LUMO level of dye molecules, finally dissociating the dye molecules. When the photon energy is not high enough to excite photocatalysts to generate reactive charge carriers and radicals, the photodegradation might occur via the photosensitization process. According to the previous

studies (Yi et al. 2014), the photodegradation of dye under visible light irradiation is not due to the direct reaction between photogenerated electron holes on the surface of catalyst and dye, but can be attributed to the photosensitization effect of the dye molecules. During this process, the MB molecules could absorb visible light in the range 450–600 nm and get excited by the visible light. Then, the electrons on the highest occupied molecular orbital (HOMO) of MB molecules transfer to the lowest unoccupied molecular orbital (LUMO) and are immediately injected to the conduction band (CB) of ZnO, whereas MB is converted to its radicals (MB•+) form. When iron ions are added into the ZnO structure, they could increase the electron capture capacity of ZnO from the photosensitizer (MB). This process could absorb more photons and effectively enhance the separation of the electron-hole pairs. The transferred electrons to the CB could react with electron acceptors such as the adsorbed O<sub>2</sub> on the surface of the catalyst to make superoxide radical anion O<sub>2</sub><sup>•-</sup>, which are further converted to HO•, H<sub>2</sub>O<sub>2</sub> and HO• species via a series of reactions. However, when the doping ratio was 3 and 5%, the formed ZnFe<sub>2</sub>O<sub>4</sub> occupies the active sites and hinders the electrons transfer to Fe<sup>3+</sup>; thus, the electron-hole pairs could not be separated effectively, so the photocatalytic activity is gradually reduced to 83.97 and 50.62% for FZ3 and FZ5, respectively (Türkyılmaz et al. 2017; Yi et al. 2014).

The photocatalytic efficiency of pure and Fe-doped ZnO was compared with the similar catalyst reported in previous investigations, the results of which are reported in Table 3. The photodegradation efficiency of MB by FZ1 was compared with Fe-doped ZnO reported in previous investigations. As can be seen, the photocatalytic efficiency of MB in the present research is 94%, indicating an improvement in the photocatalytic performance of the Fe-doped in comparison with the previously reported data for the degradation of MB. There are some research studies on using pure and/or doped ZnO for the degradation of pollutants in an aqueous solution under different irradiation light. Roguai and Djelloul prepared nanoparticles of ZnO doped with Fe (0.00, 0.02, 0.05 and 0.10) by chemical co-precipitation method and evaluated the photocatalytic activity of synthesized samples for the degradation of MB. Their results indicated that the presence of iron in the ZnO nanopowder decelerates the photocatalytic process under UV-C light

**Table 3** Comparison of the photocatalytic efficiency of ZnO and Fe-doped ZnO used to degrade pollutants in an aqueous solution

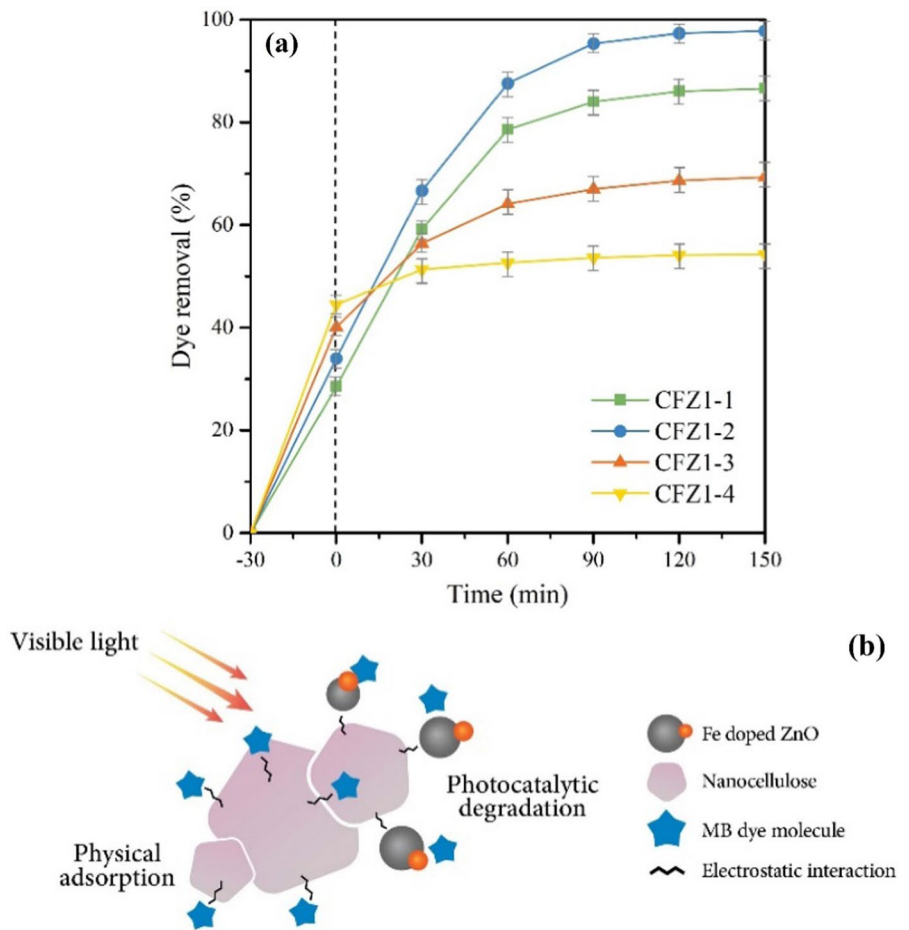
Photocatalyst	Dopant	Synthesis method	Application	Irradiation source/ time	Photo- catalytic efficiency (%)	References
ZnO	–	Hydrothermal	Methyl Orange removal	Visible light/60 min	Did not undergo decolori- zation	Shahbazkhany et al. (2020)
	–	Solvothermal	Methylene Blue removal	UV-A/120 min	19	Qi et al. (2020)
	Fe				27	
	–	Sol–gel	Methylene Blue removal	UV–Visible light/150 min	86	Isai and Shrivastava (2019)
	Fe				92	
	–	Precipitation	Direct yellow 86 removal	Sunlight/180 min	78	Kouhail et al. (2022)
	Fe				94	
	–	Precipitation	Methylene Blue removal	UV-C/120 min	91	Roguai and Djelloul (2021b)
	Fe				20	
	–	Precipitation-calci- nation	Methylene Green removal	Visible light/30 min	11	Bawazeer et al. (2021)
	Fe				91	
	–	Precipitation	Methylene Blue removal	UV-C/150 min	93	This work
	Fe			Visible light/150 min	40	
				UV-C/150 min	86	
				Visible light/150 min	94	

(Roguai and Djelloul 2021b). Isai and Shrivastava investigated the photocatalytic activity of pure and Fe-doped ZnO for photodegradation of MB under UV–visible light. Based on their obtained results, the Fe-doped ZnO had higher photocatalytic activity than pure ZnO (Isai and Shrivastava 2019). It can be concluded that a good agreement is found with the results obtained by other studies.

The prepared CFZ samples were also utilized to evaluate their dye removal performance; the results of this investigation are exhibited in Fig. 9a. Results showed that the dye removal at the dark condition was influenced by the NC content in nanocomposite. The dye removal increased with an increase in NC/Zn<sup>2+</sup> molar ratio from 0.1 to 0.4. The possible mechanism of MB degradation during this time is physical adsorption that relies on the surface hydroxyl or sulfate ester groups of NC and electrostatic attraction between NC and MB (Ganguly and Lim 2020). MB

is a positively charged cationic dye, while the surface charge of CFZs was negative; this could form a strong electrostatic interaction between them. The dye removal efficiency of CFZ1-1, CFZ1-2, CFZ1-3, and CFZ1-4 at the end of the dark time was 25.53, 33.99, 40.09 and 51.33%, respectively. Compared to other nanocomposites, CFZ1-4 with a higher molar ratio of NC to Zn<sup>2+</sup> showed the highest dye removal efficiency. The photocatalytic activity of CFZs was evaluated for MB degradation under visible light. It can be observed that the CFZ samples possessed photocatalytic ability to degrade the MB under visible light irradiation. Based on the obtained results, the performance of CFZ1-1 with a degradation efficiency of 86.61% was weaker than that of CFZ1-2 with 97.81% degradation efficiency, which was probably related to the incomplete incorporation of NC in photocatalyst particles in the CFZ1-1 sample. With further increase in the molar ratio of NC to Zn<sup>2+</sup> from

**Fig. 9** **a** MB dye removal in the presence of CFZs and **b** possible hybrid mechanism of dye removal by the nanocomposites. Error bars indicate the standard deviation measured by three independent experiments



0.2 to 0.4, there was a reduction in the degradation efficiency. This might be due to the low absorption of light by NC and the coverage of photocatalytic particles by this biopolymer which limited the photocatalytic activity of these particles. The degradation efficiency of CFZ1-3 and CFZ1-4 was 69.34 and 54.34%, respectively, which was lower than that of CFZ1-2. According to the results, the multifunctional CFZ1-2 sample showed the best combination of adsorption and photocatalytic activity among the PZ, FZs, and CFZs samples. Therefore, CFZ1-2 was used to study its photocatalytic performance for the degradation of MB in the subsequent experiments.

#### Effect of solution pH

As reported in several studies, adsorption facilitates the photocatalytic degradation process; higher adsorption results in greater effectiveness of the

photocatalysis process (Tran et al. 2021; Kumar et al. 2018). The dye molecules adsorbed on the catalyst surface are degraded faster than those in bulk due to the short life and easy annihilation of charge carriers or reactive radicals during diffusion or migration (Tran et al. 2021). By influencing the charging behavior of the catalyst and dye, the pH of the solution is an important factor that affects the dye photocatalytic degradation. The concentration of hydroxyl radicals, charge of the molecule, adsorption/desorption of the dye molecule and its intermediates onto a photocatalyst surface, and the surface charge property of the photocatalyst depend upon the pH of the dye solution. In order to determine the surface charge of CFZ1-2, the pH of zero-point charge ( $\text{pH}_{\text{pzc}}$ ) was determined (data not shown). It was obtained to be 8.1, which indicates that the surface charge of the catalyst is positive when  $\text{pH} < 8.1$  and vice versa. The solution pH was varied from 3 to 11 to study its effect



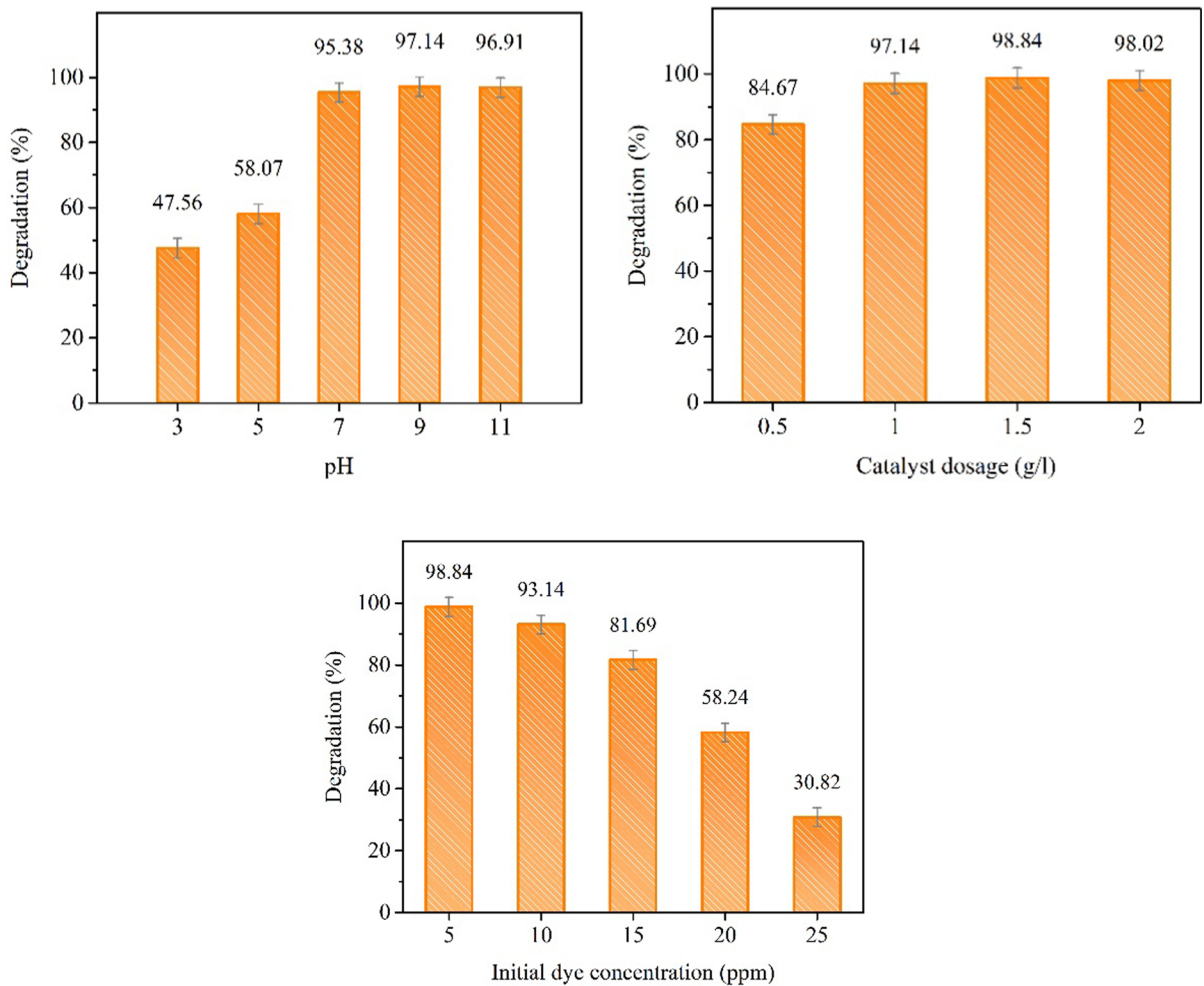


**Fig. 10** Effects of pH (a), catalyst dosage (b), and initial concentration of MB (c) on the MB degradation efficiency using CFZ1-2 (fixed experimental parameters: 1 g/L of catalyst, pH

of 9, and 5 ppm of MB at 90 min visible light irradiation). Error bars indicate the standard deviation measured by three independent experiments

on the photocatalytic degradation of the MB dye. Figure 10a indicates the effect of solution pH on the MB degradation. Results revealed that CFZ1-2 could act effectively over a wide range of pH (from 3 to 11). As expected, CFZ1-2 exhibited the highest degradation performance at pH 9, followed by pH 11, 7, 5, and 3. At acidic pH, the degradation of MB was unfavorable due to the strong electrostatic repulsion between CFZ1-2 and MB molecules. Besides, the acidic condition could increase the competitive adsorption of  $H^+$  with MB, hindering the MB access to the catalyst surface. The high degradation of MB may be resulted from the electrostatic attraction between the negative surface charge of CFZ1-2 and the positive charge of

cationic dye (MB), while the pH of the solution was above the  $pH_{pzc}$  (8.1). Thus, pH 9 was selected as the optimum pH for MB degradation.

#### Effect of nanocomposite dosage

The effect of catalyst dosage on MB degradation efficiency was studied with different amounts of CFZ1-2 (0.5 to 2.0 g/L) after 90 min irradiation under visible light. As shown in Fig. 10b, the degradation efficiency enhanced with raising the catalyst dosage up to 1.5 g/L and reduced thereafter. An explanation for the observed trend could be attributed to the number of active sites on the catalyst,

**Table 4** Comparison of the photocatalytic degradation performance of some nanocomposites used to degrade pollutants in an aqueous solution

Photocatalyst	Application	Dopant	Biopolymer	Time	Dye removal performance (%)	References	
ZnO	Methylene Blue removal	–	Cellulose nano crystal (CNC)	200 min	95.21	Abdalkarim et al. (2018)	
			Cellulose nano crystal (CNC)	300 min	79	Lefatshe et al. (2017)	
			Cellulose nano crystal (CNC)	120 min	88	Modi and Fulekar (2020)	
			Cellulose nano crystal (CNC)	240 min	93.55	Guan et al. (2019)	
			Regenerated cellulose (RC)	150 min	85.30	Fu et al. (2017)	
			Micro crystalline cellulose (MCC)	120 min	90	Zuo et al. (2014)	
			Chitosan	180 min	78	Li et al. (2021a, b)	
			Reduced graphene oxide (rGO)	60 min	87	Asgharian et al. (2019)	
	Methyl orange removal	–	Fe/Ni	Chitosan	150 min	92	Nawaz et al. (2020)
			Au	Starch	90 min	87.75	Peychev and Vasileva (2021)
	Tetracycline removal	–	Al	Micro/nano cellulose fibers (MNCF)	180 min	54	Li et al. (2020)
			Al	Micro/nano cellulose fibers (MNCF)	180 min	85	
	Eyosin	–	Fe	Nanofibrillated cellulose (NFC)	120 min	90	Xiao et al. (2017)
Methylene Blue removal	–	Au	Cellulose acetate (CA)	180 min	87	Abad et al. (2020)	
Methylene Blue removal	–	Fe	Nanocellulose (NC)	120 min	98.84	This work	

which enhanced with the addition of the photocatalyst, improving the degradation efficiency. However, an increase of the catalyst dosage to over 1.5 g/L had negative effect on the catalyst performance and led to the reduction of the degradation efficiency of CFZ1-2. It seems that the enhancement of catalyst amounts could lead to the agglomeration of photocatalyst particles, light scattering, and hindering the light transmission, hindering the photocatalytic performance (Emadian et al. 2020; Mirzaeifard et al. 2020). Based on the results, the optimum dosage of CFZ1-2 for MB degradation was selected at 1.5 g/L for the subsequent experiments.

#### Effect of initial dye concentration

The influence of initial dye concentration (5–25 ppm) on dye degradation by 1.5 g/L of the CFZ1-2

photocatalyst at pH 9 was studied. As can be observed in Fig. 10c, by increasing the dye concentration, the photocatalytic degradation indicated a downward trend. At a constant amount of catalyst, the number of active sites in the catalyst reduced upon dye adsorption onto the surface of catalyst, resulting in a decrease in the active radical production and also reduction of degradation of efficiency. Furthermore, when the MB concentration was increased, the turbidity of reaction mixture also increased that acted as a screen against visible light, prevented the light photons from reaching the active sites of the catalyst and deteriorated the photocatalytic degradation (Raja et al. 2020).

The photocatalytic efficiency of different nanocomposites based on ZnO for the degradation of various pollutants is summarized in Table 4. It is notable that although there are some research studies on using

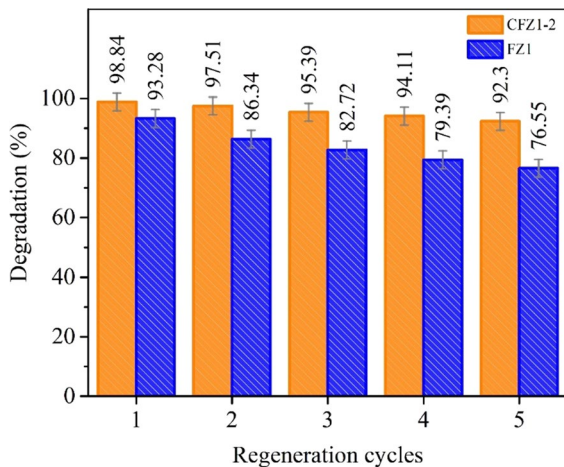


**Fig. 11** Recycling photocatalyst tests for CFZ1-2 and FZ1 under optimum conditions. Error bars indicate the standard deviation measured by three independent experiments

pure and/or doped ZnO nanocomposites as efficient photocatalysts, few studies have been done on the fabrication and application of Fe-doped ZnO/nanocellulose composite as photocatalyst. The degradation efficiency of MB by the CFZ1-2 nanocomposite was compared with other composites reported in previous investigations. As can be seen, the degradation efficiency of MB in the present research is 98.84%, indicating an improvement in the photocatalytic performance of the CFZ1-2 in comparison with the previously reported data for the degradation of MB. Therefore, the present nanocomposite is a suitable option for dye degradation in wastewater treatment.

### Regeneration

The reusability and stability of a photocatalyst are critical parameters for its practical application. The reusability of the CFZ1-2 and FZ1 was investigated under optimized conditions for the MB degradation (pH 9, catalyst dosage = 1.5 g/L, and MB initial concentration = 5 ppm). The reusability tests were done by centrifuging the CFZ1-2 and FZ1 samples from the first cycle, which were then washed and oven-dried at 50 °C. Figure 11 illustrates that the degradation efficiency of the CFZ1-2 and FZ1 samples slightly decreased from 98.84% to 92.31% and 93.28% to 76.5% during the different reuse runs, respectively. In fact, the degradation efficiency of CFZ1-2 and FZ1 was kept higher than 92 and 76%

after five successive runs, respectively. It can be concluded that compared to the FZ1, the CFZ1-2 exhibited remarkable recyclability and its photocatalytic performance did not decrease significantly after five cycles. This result can be attributed to the existence of nanocellulose as a suitable support for Fe doped ZnO that facilitated the recovery process and improved its reusability. The negligible reduction of degradation efficiency of CFZ1-2 might be attributed to the trapping of MB molecules on the active sites of the catalyst surface and the loss of the catalyst throughout the cycling experiments. The obtained result confirms that the CFZ1-2 is a promising catalyst for long-term uses in industrial wastewater treatment processes.

### Conclusion

In this study, spherical NC was successfully isolated from broomcorn stalk, characterized and used to prepare NC/Fe-doped ZnO (CFZ) nanocomposite through a facile *in-situ* method. The fabricated samples (PZ, FZs and CFZs) were characterized by various techniques and used for the photocatalytic degradation of MB. The comparison of PZ and FZs photocatalytic performance in the presence of visible light showed that the presence of Fe<sup>3+</sup> in ZnO matrix effectively increased the ZnO photocatalytic performance. The degradation efficiency of FZ1 was about 94.21% at 150 min, which was higher than that of PZ (36.96%) in the same duration. The higher degradation efficiency of FZ1 could be related to the decreased bandgap of Fe-doped ZnO compared to pure ZnO which led to enhanced absorbance of photons under the visible light and inhibited the recombination of electron/hole pairs. The FZ1 was then conjugated with isolated NC at varying NC/Zn<sup>2+</sup> molar ratios. The crystalline size of FZ1 was affected by the addition of NC. The crystalline size of CFZs was smaller than that of FZ1. The photocatalytic activity of CFZs was evaluated for MB degradation under visible light. Compared with PZ and FZs, the synthesized CFZs indicated superior photocatalytic performance in shorter time because the presence of NC as a matrix could disperse Fe-doped ZnO particles and avoid agglomeration and aggregation. The highest degradation efficiency was achieved by CFZ1-2 and its photocatalytic performance was evaluated at different pH, photocatalyst dosages, and

initial MB concentrations. It was observed that a maximum MB degradation of 98.84% was achieved by 15 g/L CFZ1-2 in 5 ppm MB solution at pH 9 in 120 min under visible irradiation. The photocatalytic efficiency of the CFZ1-2 and FZ1 was examined up to five cycles and compared. The CFZ1-2 was able to preserve its original performance with more than 92% degradation efficiency even on reuse and it was higher than that of FZ1. This result can be attributed to the existence of nanocellulose in CFZ1-2 as a suitable support for Fe-doped ZnO that facilitated the recovery process and improved its reusability. Hence, CFZ1-2 can be regarded as a great photocatalyst nanocomposite for the enhanced degradation of cationic dye impurities under visible light irradiation.

**Acknowledgments** The authors are grateful to Process Design Research laboratory for providing the experimental instruments.

**Funding** This work was supported by Babol Noshirvani University of Technology (BNUT) through the postgraduate student Grant number BNUT/964115043.

#### Declarations

**Conflict of interests** We declare we have no competing interests.

#### References

- Abad SNK, Mozammel M, Moghaddam J et al (2020) Highly porous, flexible and robust cellulose acetate/Au/ZnO as a hybrid photocatalyst. *Appl Surf Sci* 526:146237. <https://doi.org/10.1016/j.apsusc.2020.146237>
- Abdalkarim SYH, Yu H-Y, Wang C et al (2018) Green synthesis of sheet-like cellulose nanocrystal–zinc oxide nanohybrids with multifunctional performance through one-step hydrothermal method. *Cellulose* 25:6433–6446. <https://doi.org/10.1007/s10570-018-2011-0>
- Abdel-Wahab MS, Jilani A, Yahia I et al (2016) Enhanced the photocatalytic activity of Ni-doped ZnO thin films: morphological, optical and XPS analysis. *Superlattices Microstruct* 94:108–118. <https://doi.org/10.1016/j.spmi.2016.03.043>
- Abebe B, Ananda Murthy HC, Zerefa E et al (2020) Porous PVA/Zn–Fe–Mn oxide nanocomposites: methylene blue dye adsorption studies. *Mater Res Express* 7:065002. <https://doi.org/10.1088/2053-1591/ab94fc>
- Akir S, Barras A, Coffinier Y et al (2016) Eco-friendly synthesis of ZnO nanoparticles with different morphologies and their visible light photocatalytic performance for the degradation of Rhodamine B. *Ceram Int* 42:10259–10265. <https://doi.org/10.1016/j.ceramint.2016.03.153>
- Ali A, Shoeb M, Li Y et al (2021) Enhanced photocatalytic degradation of antibiotic drug and dye pollutants by graphene-ordered mesoporous silica (SBA 15)/TiO<sub>2</sub> nanocomposite under visible-light irradiation. *J Mol Liq* 324:114696. <https://doi.org/10.1016/j.molliq.2020.114696>
- Asgharian M, Mehdipourghazi M, Khoshandam B et al (2019) Photocatalytic degradation of methylene blue with synthesized rGO/ZnO/Cu. *Chem Phys Lett* 719:1–7. <https://doi.org/10.1016/j.cplett.2019.01.037>
- Ba-Abbad MM, Kadhun AAH, Mohamad AB et al (2013) Visible light photocatalytic activity of Fe<sup>3+</sup>-doped ZnO nanoparticle prepared via sol–gel technique. *Chemosphere* 91:1604–1611. <https://doi.org/10.1016/j.chemosphere.2012.12.055>
- Bawazeer TM, Alsoufi MS, Shkir M et al (2021) Excellent improvement in photocatalytic nature of ZnO nanoparticles via Fe doping content. *Inorg Chem Commun* 130:108668. <https://doi.org/10.1016/j.inoche.2021.108668>
- Chand P, Singh V, Kumar D (2020) Rapid visible light-driven photocatalytic degradation using Ce-doped ZnO nanocatalysts. *Vacuum* 178:109364. <https://doi.org/10.1016/j.vacuum.2020.109364>
- Chiu Y-H, Chang T-FM, Chen C-Y et al (2019) Mechanistic insights into photodegradation of organic dyes using heterostructure photocatalysts. *Catalysts* 9:430. <https://doi.org/10.3390/catal9050430>
- Ciciliati MA, Silva MF, Fernandes DM et al (2015) Fe-doped ZnO nanoparticles: synthesis by a modified sol–gel method and characterization. *Mater Lett* 159:84–86. <https://doi.org/10.1016/j.matlet.2015.06.023>
- Elfeky AS, Salem SS, Elzeref AS et al (2020) Multifunctional cellulose nanocrystal/metal oxide hybrid, photo-degradation, antibacterial and larvicidal activities. *Carbohydr Polym* 230:115711. <https://doi.org/10.1016/j.carbpol.2019.115711>
- Emadian SS, Ghorbani M, Bakeri G (2020) Magnetically separable CoFe<sub>2</sub>O<sub>4</sub>/ZrO<sub>2</sub> nanocomposite for the photocatalytic reduction of hexavalent chromium under visible light irradiation. *Synth Metals* 267:116470. <https://doi.org/10.1016/j.synthmet.2020.116470>
- Evdokimova O, Fedulova A, Evdokimova A et al (2020) Preparation of hybrid nanocomposites based on nanoscale cellulose and magnetic nanoparticles with photocatalytic properties. *Inorg Mater Appl Res* 11:371–376. <https://doi.org/10.1134/S2075113320020100>
- Fabbiyola S, Kennedy LJ, Ratnaji T et al (2016) Effect of Fe-doping on the structural, optical and magnetic properties of ZnO nanostructures synthesised by co-precipitation method. *Ceram Int* 42:1588–1596. <https://doi.org/10.1016/j.ceramint.2015.09.110>
- Flores K, Valdes C, Ramirez D et al (2020) The effect of hybrid zinc oxide/graphene oxide (ZnO/GO) nano-catalysts on the photocatalytic degradation of simazine. *Chemosphere* 259:127414. <https://doi.org/10.1016/j.chemosphere.2020.127414>
- Fu F, Gu J, Xu X et al (2017) Interfacial assembly of ZnO–cellulose nanocomposite films via a solution process: a one-step biomimetic approach and excellent photocatalytic properties. *Cellulose* 24:147–162. <https://doi.org/10.1007/s10570-016-1087-7>

- Ganguly K, Lim K-T (2020) Nanocellulose-based polymer nanohybrids and nanocomposite applications. In: Abd-El Salam K (ed) Multifunctional hybrid nanomaterials for sustainable agri-food and ecosystems. Elsevier, Amsterdam, pp 485–504
- Ghasemlou M, Daver F, Ivanova EP et al (2021) Surface modifications of nanocellulose: from synthesis to high-performance nanocomposites. *Prog Polym Sci* 119:101418. <https://doi.org/10.1016/j.progpolymsci.2021.101418>
- Guan Y, Yu H-Y, Abdalkarim SYH et al (2019) Green one-step synthesis of ZnO/cellulose nanocrystal hybrids with modulated morphologies and superfast absorption of cationic dyes. *Int J Biol Macromol* 132:51–62. <https://doi.org/10.1016/j.ijbiomac.2019.03.104>
- Isai KA, Shrivastava VS (2019) Photocatalytic degradation of methylene blue using ZnO and 2% Fe–ZnO semiconductor nanomaterials synthesized by sol–gel method: a comparative study. *SN Appl Sci* 1:1–11. <https://doi.org/10.1007/s42452-019-1279-5>
- Jiang Y, Lawan I, Zhou W et al (2020) Synthesis, properties and photocatalytic activity of a semiconductor/cellulose composite for dye degradation—a review. *Cellulose* 27:595–609. <https://doi.org/10.1007/s10570-019-02851-w>
- Kamal T, Ul-Islam M, Khan SB et al (2015) Adsorption and photocatalyst assisted dye removal and bactericidal performance of ZnO/chitosan coating layer. *Int J Biol Macromol* 81:584–590. <https://doi.org/10.1016/j.ijbiomac.2015.08.060>
- Kim D, Yong K (2021) Boron doping induced charge transfer switching of a C3N4/ZnO photocatalyst from Z-scheme to type II to enhance photocatalytic hydrogen production. *Appl Catal B* 282:119538. <https://doi.org/10.1016/j.apcatb.2020.119538>
- Kouhail M, El Ahmadi Z, Benayada A (2022) Effect of Ag, Ca, and Fe on photocatalytic activity of ZnO nanoparticles to remove textile dyes under sunlight irradiation. *React Kinet Mech Catal* 135:169–182. <https://doi.org/10.1007/s11144-021-02061-1>
- Kumar SG, Rao KK (2015) Zinc oxide based photocatalysis: tailoring surface-bulk structure and related interfacial charge carrier dynamics for better environmental applications. *RSC Adv* 5:3306–3351. <https://doi.org/10.1039/C4RA13299H>
- Kumar A, Kumar A, Sharma G et al (2018) Quaternary magnetic BiOCl/g-C3N4/Cu2O/Fe3O4 nano-junction for visible light and solar powered degradation of sulfamethoxazole from aqueous environment. *J Chem Eng* 334:462–478. <https://doi.org/10.1016/j.cej.2017.10.049>
- Langari MM, Nikzad M, Ghoreyshi AA et al (2019) Isolation of nanocellulose from broomcorn stalks and its application for nanocellulose/xanthan film preparation. *ChemistrySelect* 4:11987–11994. <https://doi.org/10.1002/slct.201902533>
- Lavand AB, Malghe YS (2018) Synthesis, characterization and visible light photocatalytic activity of carbon and iron modified ZnO. *J King Saud Univ Sci* 30:65–74. <https://doi.org/10.1016/j.jksus.2016.08.009>
- Lefatshe K, Muiva CM, Kebaabetswe LP (2017) Extraction of nanocellulose and in-situ casting of ZnO/cellulose nanocomposite with enhanced photocatalytic and antibacterial activity. *Carbohydr Polym* 164:301–308. <https://doi.org/10.1016/j.carbpol.2017.02.020>
- Li H, Zhang L, Lu H et al (2020) Macro-/nanoporous Al-doped ZnO/cellulose composites based on tunable cellulose fiber sizes for enhancing photocatalytic properties. *Carbohydr Polym* 250:116873. <https://doi.org/10.1016/j.carbpol.2020.116873>
- Li H, Hao M-X, Kang H-R et al (2021a) Facile production of three-dimensional chitosan fiber embedded with zinc oxide as recoverable photocatalyst for organic dye degradation. *Int J Biol Macromol* 181:150–159. <https://doi.org/10.1016/j.ijbiomac.2021.03.157>
- Li X, Zhang L, Wang Z et al (2021b) Cellulose controlled zinc oxide nanoparticles with adjustable morphology and their photocatalytic performances. *Carbohydr Polym* 259:117752. <https://doi.org/10.1016/j.carbpol.2021.117752>
- Lizundia E, Goikuria U, Vilas JL et al (2018) Metal nanoparticles embedded in cellulose nanocrystal based films: Material properties and post-use analysis. *Biomacromol* 19:2618–2628. <https://doi.org/10.1021/acs.biomac.8b00243>
- Masoudnia S, Juybari MH, Mehrabian RZ et al (2020) Efficient dye removal from wastewater by functionalized macromolecule chitosan-SBA-15 nanofibers for biological approaches. *Int J Biol Macromol* 165:118–130. <https://doi.org/10.1016/j.ijbiomac.2020.09.158>
- Mirzaeifard Z, Shariatnia Z, Jourshabani M et al (2020) ZnO photocatalyst revisited: effective photocatalytic degradation of emerging contaminants using S-doped ZnO nanoparticles under visible light radiation. *Ind Eng Chem Res* 59:15894–15911. <https://doi.org/10.1021/acs.iecr.0c03192>
- Modi S, Fulekar M (2020) Synthesis and characterization of zinc oxide nanoparticles and zinc oxide/cellulose nanocrystals nanocomposite for photocatalytic degradation of Methylene blue dye under solar light irradiation. *Nanotechnol Environ Eng* 5:1–12. <https://doi.org/10.1007/s41204-020-00080-2>
- Moon RJ, Martini A, Nairn J et al (2011) Cellulose nanomaterials review: structure, properties and nanocomposites. *Chem Soc Rev* 40:3941–3994. <https://doi.org/10.1039/C0CS00108B>
- Muniyasamy A, Sivaporul G, Gopinath A et al (2020) Process development for the degradation of textile azo dyes (mono-, di-, poly-) by advanced oxidation process-Ozonation: Experimental & partial derivative modelling approach. *J Environ Manag* 265:110397. <https://doi.org/10.1016/j.jenvman.2020.110397>
- Nagaraju P, Puttaiah SH, Wantala K et al (2020) Preparation of modified ZnO nanoparticles for photocatalytic degradation of chlorobenzene. *Appl Water Sci* 10:1–15. <https://doi.org/10.1007/s13201-020-01228-w>
- Namini AS, Delbari SA, Mousavi M et al (2021) Synthesis and characterization of novel ZnO/NiCr2O4 nanocomposite for water purification by degradation of tetracycline and phenol under visible light irradiation. *Mater Res Bull* 139:111247. <https://doi.org/10.1016/j.materresbull.2021.111247>
- Nang An V, Van TT, Nhan HT et al (2020) Investigating methylene blue adsorption and photocatalytic activity of ZnO/

- CNC nanohybrids. *J Nanomater.* <https://doi.org/10.1155/2020/6185976>
- Nawaz A, Khan A, Ali N et al (2020) Fabrication and characterization of new ternary ferrites-chitosan nanocomposite for solar-light driven photocatalytic degradation of a model textile dye. *Environ Technol Innov* 20:101079. <https://doi.org/10.1016/j.eti.2020.101079>
- Pechev B, Vasileva P (2021) Novel starch-mediated synthesis of Au/ZnO nanocrystals and their photocatalytic properties. *Heliyon* 7:e07402. <https://doi.org/10.1016/j.heliyon.2021.e07402>
- Qi K, Cheng B, Yu J et al (2017) Review on the improvement of the photocatalytic and antibacterial activities of ZnO. *J Alloys Compd* 727:792–820. <https://doi.org/10.1016/j.jallcom.2017.08.142>
- Qi K, Xing X, Zada A et al (2020) Transition metal doped ZnO nanoparticles with enhanced photocatalytic and antibacterial performances: experimental and DFT studies. *Ceram Int* 46:1494–1502. <https://doi.org/10.1016/j.ceramint.2019.09.116>
- Raja A, Rajasekaran P, Selvakumar K et al (2020) Visible active reduced graphene oxide-BiVO<sub>4</sub>-ZnO ternary photocatalyst for efficient removal of ciprofloxacin. *Sep Purif Technol* 233:115996. <https://doi.org/10.1016/j.seppur.2019.115996>
- Rajendran S, Naushad M, Ponce LC et al (2020) Green photocatalysts for energy and environmental process. Springer, Cham
- Roguai S, Djelloul A (2021a) Photocatalytic degradation of methylene blue using sprayed Mg diluted ZnO heterostructure thin films photocatalysts. *React Kinet Mech Catal* 132:1225–1244. <https://doi.org/10.1007/s11144-021-01963-4>
- Roguai S, Djelloul A (2021b) Structural, microstructural and photocatalytic degradation of methylene blue of zinc oxide and Fe-doped ZnO nanoparticles prepared by simple coprecipitation method. *Solid State Commun* 334:114362. <https://doi.org/10.1016/j.ssc.2021.114362>
- Saffari R, Shariatnia Z, Jourshabani M (2020) Synthesis and photocatalytic degradation activities of phosphorus containing ZnO microparticles under visible light irradiation for water treatment applications. *Environ Pollut* 259:113902. <https://doi.org/10.1016/j.envpol.2019.113902>
- Saleh R, Prakoso SP, Fishli A (2012) The influence of Fe doping on the structural, magnetic and optical properties of nanocrystalline ZnO particles. *J Magn Magn Mater* 324:665–670. <https://doi.org/10.1016/j.jmmm.2011.07.059>
- Saxena M, Sharma N, Saxena R (2020) Highly efficient and rapid removal of a toxic dye: Adsorption kinetics, isotherm, and mechanism studies on functionalized multiwalled carbon nanotubes. *Surf Interfaces* 21:100639. <https://doi.org/10.1016/j.surfin.2020.100639>
- Senthil Kumar M, Arunagiri C (2021) Efficient photocatalytic degradation of organic dyes using Fe-doped ZnO nanoparticles. *J Mater Sci Mater Electron* 32:17925–17935. <https://doi.org/10.1007/s10854-021-06328-0>
- Shahbazkhany S, Salehi M, Mousavi-Kamazani M (2020) Facile synthesis, characterization, and decolorization activity of Mn<sup>2+</sup> and Al<sup>3+</sup> co-doped hexagonal-like ZnO nanostructures as photocatalysts. *Appl Organomet Chem* 34:e5346. <https://doi.org/10.1002/aoc.5346>
- Sharma M, Poddar M, Gupta Y et al (2020) Solar light assisted degradation of dyes and adsorption of heavy metal ions from water by CuO–ZnO tetrapodal hybrid nanocomposite. *Mater Today Chem* 17:100336. <https://doi.org/10.1016/j.mtchem.2020.100336>
- Shi C, Zhang L, Bian H et al (2021) Construction of Ag–ZnO/cellulose nanocomposites via tunable cellulose size for improving photocatalytic performance. *J Clean Prod* 288:125089. <https://doi.org/10.1016/j.jclepro.2020.125089>
- Sirajudheen P, Karthikeyan P, Vigneshwaran S et al (2020) Synthesis and characterization of La (III) supported carboxymethylcellulose-clay composite for toxic dyes removal: Evaluation of adsorption kinetics, isotherms and thermodynamics. *Int J Biol Macromol* 161:1117–1126. <https://doi.org/10.1016/j.ijbiomac.2020.06.103>
- Tran VA, Nguyen TLH, Doan V-D (2021) Fabrication of Fe<sub>3</sub>O<sub>4</sub>/CuO@C composite from MOF-based materials as an efficient and magnetically separable photocatalyst for degradation of ciprofloxacin antibiotic. *Chemosphere* 270:129417. <https://doi.org/10.1016/j.chemosphere.2020.129417>
- Türkyılmaz ŞŞ, Güy N, Özacar M (2017) Photocatalytic efficiencies of Ni, Mn, Fe and Ag doped ZnO nanostructures synthesized by hydrothermal method: the synergistic/antagonistic effect between ZnO and metals. *J Photochem Photobiol A* 341:39–50. <https://doi.org/10.1016/j.jphotochem.2017.03.027>
- Wahid F, Duan Y-X, Hu X-H et al (2019) A facile construction of bacterial cellulose/ZnO nanocomposite films and their photocatalytic and antibacterial properties. *Int J Biol Macromol* 132:692–700. <https://doi.org/10.1016/j.ijbiomac.2019.03.240>
- Wang R, Hao Q, Feng J et al (2019) Enhanced separation of photogenerated charge carriers and catalytic properties of ZnO–MnO<sub>2</sub> composites by microwave and photothermal effect. *J Alloys Compd* 786:418–427. <https://doi.org/10.1016/j.jallcom.2019.02.009>
- Wang Y, Geng Q, Yang J et al (2020) Hybrid system of flocculation-photocatalysis for the decolorization of crystal violet, reactive red X-3B, and acid orange II dye. *ACS Omega* 5:31137–31145. <https://doi.org/10.1021/acsomega.0c04285>
- Xiao H, Zhang W, Wei Y et al (2017) Fabrication of Fe/ZnO composite nanosheets by nanofibrillated cellulose as soft template and photocatalytic degradation of tetracycline. *J Inorg Organomet Polym Mater* 28:1299–1304. <https://doi.org/10.1007/s10904-017-0712-8>
- Xiao H, Zhang W, Wei Y et al (2018) Carbon/ZnO nanorods composites templated by TEMPO-oxidized cellulose and photocatalytic activity for dye degradation. *Cellulose* 25:1809–1819. <https://doi.org/10.1007/s10570-018-1651-4>
- Yang C, Xu W, Nan Y et al (2020) Fabrication and characterization of a high performance polyimide ultrafiltration membrane for dye removal. *J Colloid Interface Sci* 562:589–597. <https://doi.org/10.1016/j.jcis.2019.11.075>
- Yi S, Cui J, Li S et al (2014) Enhanced visible-light photocatalytic activity of Fe/ZnO for rhodamine B degradation and

- its photogenerated charge transfer properties. *Appl Surf Sci* 319:230–236. <https://doi.org/10.1016/j.apsusc.2014.06.151>
- Yu J, Yu X (2008) Hydrothermal synthesis and photocatalytic activity of zinc oxide hollow spheres. *Environ Sci Technol* 42:4902–4907. <https://doi.org/10.1021/es800036n>
- Zhang B, Yang D, Qiu X et al (2020) Fabricating ZnO/lignin-derived flower-like carbon composite with excellent photocatalytic activity and recyclability. *Carbon* 162:256–266. <https://doi.org/10.1016/j.carbon.2020.02.038>
- Zuo H-F, Guo Y-R, Li S-J et al (2014) Application of micro-crystalline cellulose to fabricate ZnO with enhanced photocatalytic activity. *J Alloys Compd* 617:823–827. <https://doi.org/10.1016/j.jallcom.2014.08.071>

**Publisher's Note** Springer Nature remains neutral with regard to jurisdictional claims in published maps and institutional affiliations.